Accepted Manuscript

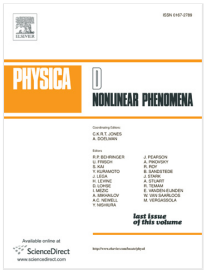

Flow transitions resembling bifurcations of the logistic map in simulations of the baroclinic rotating annulus

R.M.B. Young, P.L. Read

PII: S0167-2789(08)00059-6
DOI: 10.1016/j.physd.2008.02.014
Reference: PHYSD 30346

To appear in: *Physica D*

Received date: 5 March 2007
Revised date: 29 January 2008
Accepted date: 5 February 2008

Please cite this article as: R.M.B. Young, P.L. Read, Flow transitions resembling bifurcations of the logistic map in simulations of the baroclinic rotating annulus, *Physica D* (2008), doi:10.1016/j.physd.2008.02.014

Flow transitions resembling bifurcations of the logistic map in simulations of the baroclinic rotating annulus

R. M. B. Young *, P. L. Read

Atmospheric, Oceanic and Planetary Physics, Department of Physics, University of Oxford, UK

Abstract

We present evidence for a sequence of bifurcations in simulations of the differentially heated baroclinic rotating annulus, similar to bifurcations associated with the logistic map. The Met. Office / Oxford Rotating Annulus Laboratory Simulation (`MORALS`) code is used to construct a detailed numerical regime diagram for the annulus, and the distribution of regimes in parameter space is discussed. The bifurcations are observed in a sequence of runs at high temperature forcing, identified by Poincaré sections of the dominant temperature mode amplitude time series. Higher order return maps and predictions using quadratic fits to the data are used to verify this result, and Lyapunov exponents are calculated to identify and quantify the chaotic parts of the sequence.

Key words: baroclinic, rotating annulus, chaos, logistic map

PACS: 47.20.Ky, 05.45.Pq, 47.32.Ef, 05.45.Tp

Preprint submitted to Physica D *29 March 2008*

1 Introduction

The differentially heated rotating annulus [1–3] is a laboratory experiment that has been used for over 50 years to produce behaviour qualitatively similar to the midlatitudes of a generic planetary atmosphere. The experiment consists of two concentric cylinders maintained at different temperatures, rotating about a vertical axis, with fluid between them (Fig. 1). This setup is firmly established as an insightful laboratory analogue for certain kinds of atmospheric dynamical behaviour, and is also a useful testbed for the methods used to study them.

Fig. 1. Schematic of the rotating annulus setup (to scale), with inner and outer cylinders at temperatures T_a and T_b respectively, rotating at constant angular velocity Ω. Fluid is contained between the cylinders.

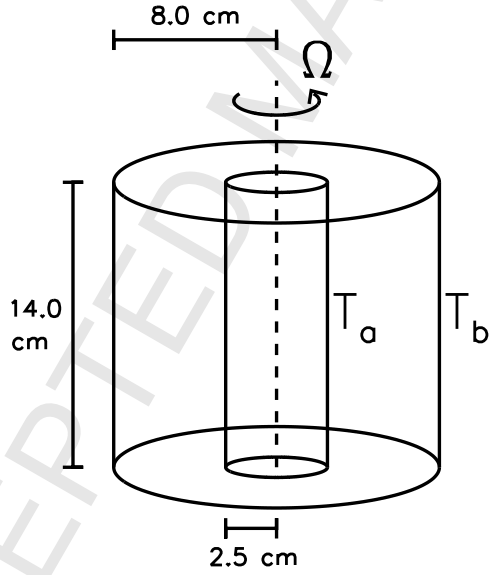

* Address for correspondence: Atmospheric, Oceanic and Planetary Physics, Clarendon Laboratory, Parks Road, Oxford OX1 3PU, United Kingdom, +44 01865 272258 (phone), +44 01865 272923 (fax).

Email address: r.young1@physics.ox.ac.uk (R. M. B. Young).

URL: http://www.atm.ox.ac.uk/user/young/ (R. M. B. Young).

Baroclinic instability, which is one of the primary mechanisms governing large scale fluid motion in the atmosphere, can be reproduced in the annulus under certain conditions when a temperature gradient is combined with rotation [1], and the laboratory setting allows this to be studied in a controlled and reproducible environment. As well as similarities with the atmosphere, the annulus displays a rich and diverse range of behaviour worthy of study in its own right, including low–dimensional dynamics. Although using the annulus as a direct analogue of the highly turbulent Earth's atmosphere may be questionable, the complex nature of real atmospheres means we need simpler analogues for testing ideas and methods. Weakly turbulent behaviour observed in the annulus is more relevant for simpler planetary atmospheres such as on Mars, where the large–scale flow is believed to be more predictable than large-scale flow on Earth [4].

This work is exclusively a computational study. Initially, we summarize the construction of a detailed numerical regime diagram for the rotating annulus; this is directly comparable with equivalent diagrams produced from earlier laboratory experiments. We then report the discovery of a previously unseen regime, whose behaviour is similar to the bifurcations produced by iteration of the logistic map [5–7]. In the laboratory, this type of behaviour is well documented in Rayleigh–Bénard convection cells using water and mercury: these experiments found period–doubling bifurcations in velocity and temperature time series as a result of varying external forcing, either by a temperature gradient (water) [8, 9] or magnetic forcing (mercury) [10, 11]. Period–doubling of a periodic amplitude modulation has also been seen as a result of baroclinic instability in a two layer, open cylinder experiment driven by differential rotation [12]. It has not been observed to date in the laboratory annulus under

radial thermal forcing, however.

Section 2 describes the simulation. In Section 3 the regime diagram and its main features are outlined. We present evidence for a sequence of bifurcations similar to the logistic map in Section 4, and supplementary evidence using Lyapunov exponents in Section 5. Section 6 provides discussion and conclusions.

2 The simulation

We use the Met. Office / Oxford Rotating Annulus Laboratory Simulation (`MORALS`) code [13–15]. This solves the full Navier–Stokes, continuity, and heat transfer equations along with equations of state for density, viscosity and thermal diffusivity (Appendix A), under the Boussinesq approximation for a cylindrical annulus rotating at angular velocity Ω. The equations are cast in velocity–temperature–pressure form: u (meridional), v (zonal) and w (vertical) velocities / cm s^{-1}, temperature T / °C and a normalized pressure $\Pi = P/\rho_0$ / cm^2 s^{-2}. In this work we use the 'standard' configuration with inner and outer walls maintained at constant temperatures T_a and T_b respectively, with no internal heating, and include a rigid lid (i.e., a no–slip upper boundary condition). The model works on a (R, ϕ, z) grid of $24 \times 64 \times 24$ nodes stretched in R and z (to resolve the boundary layers). The parameters defining the annulus and working fluid (Table 1) are identical to the 'main comparison' of Hignett et al. [14], but use a range of Ω and $\Delta T = T_b - T_a$, instead of just one value.

Table 1

Parameters defining the annulus apparatus and fluid properties.

Annulus inner cylinder radius	a = 2.5 cm
Annulus outer cylinder radius	b = 8.0 cm
Annulus height	d = 14.0 cm
Working fluid (by volume)	83% water / 17% glycerol
Mean density	$\rho_0 = 1.044$ g cm^{-3}
Volume expansion coefficient	$\alpha = 2.86 \times 10^{-4}$ / K^{-1}
Prandtl number	Pr = 13.1
Rotation rates	$0.19 \leq \Omega /$ rads$^{-1} \leq 3.50$
Inner wall temperatures	$12.5 \leq T_a/^\circ\mathrm{C} \leq 19.995$
Outer wall temperatures	$20.005 \leq T_b/^\circ\mathrm{C} \leq 27.5$
Temperature differences	$0.01 \leq \Delta T /$ K ≤ 15
Initial temperature	$T_0 = 20^\circ$C (midway from T_a to T_b)

3 Numerical regime diagram

Eighty–two simulations were run to construct a numerical regime diagram. Each run was placed in the regime diagram using the thermal Rossby and Taylor numbers:

$$\Theta \equiv \frac{g\alpha\Delta T d}{\Omega^2 (b-a)^2} \qquad \mathcal{T} \equiv \frac{4\Omega^2 (b-a)^5}{\nu^2 d},$$

where g is the gravitational acceleration and ν is the kinematic viscosity. These parameters have been used for some decades as the standard quantities for comparing annulus flow regimes, and so will allow comparison between our results and earlier work. Both Θ and $\mathcal{T}$ are dimensionless parameters representing the balance of forces in the annulus. The thermal Rossby number Θ is the ratio between buoyancy/inertial forces and Coriolis forces; at large Θ rotation may be ignored, and at low Θ the geostrophic approximation is justified. The Taylor number $\mathcal{T}$ is the ratio between inertial forces due to rotation, and viscous forces; it measures the ability of a fluid to resist shear stresses. Using the values in Table 1,

$$\Theta = 0.130\ \frac{\Delta T}{\Omega^2} \qquad \mathcal{T} = 5.22 \times 10^6\ \Omega^2.$$

The simulations were initialized by first running a reduced model, which integrates the axisymmetric form of the equations of motion over a vertical 2D slice (with the same parameters as the subsequent 3D run). This was run until a steady state was reached (around $t = 10,000$s). The slice was then copied to each azimuthal coordinate, and a sinusoidal perturbation was introduced

to the temperature field, defined by

$$\delta T(R,\phi,z) = \begin{cases} X \sin\left(\frac{R-a}{b-a}\pi\right) \sin\left(\frac{z}{d}\pi\right) & \phi = 0 \\ 0 & \text{otherwise,} \end{cases}$$

where $X = 0.1$ K. Note that this perturbation is applied only at $\phi = 0$, so it is essentially a white noise perturbation independent of any particular azimuthal behaviour. Each simulation starts from a different axisymmetric state (defined by the 2D run), but is initialized using the same perturbation. The perturbation is necessary to move the system away from an (unstable) axisymmetric state, as it would otherwise remain axisymmetric (N.B.: the effects of using finite precision arithmetic would eventually grow to appreciable levels, causing the symmetry to be broken, but this would take a long time).

Each simulation was run at constant ΔT and Ω until transient motion had decayed and a flow regime was identified. This process took between 1500 and 13500 seconds of simulated time, depending on the parameters. Spatial Fourier transforms of the temperature and pressure fields around an azimuthal circle at mid height and mid radius were saved every 1–2s. Complete velocity, temperature, and pressure fields were saved every 100–300s. Each run was classified using a number of methods, illustrated in Fig. 2. A wavenumber spectrum (Fig. 2a) containing the instantaneous amplitudes of each temperature mode allows the dominant wavenumber M to be identified. The dominant wavenumber M of the fluid at time t is the azimuthal mode (in any quantity one chooses) with the largest amplitude at time t, ignoring wavenumber zero. It can also be identified by eye from the rotational symmetry of the fluid: for azimuthal wavenumber M the variation in any given quantity repeats after

Fig. 2. Characteristics of wavenumber-3 amplitude vacillation for a 9000 s run with $\Omega = 0.80$ rad s^{-1}, $\Delta T = 5$ K, $\mathcal{T} = 3.34 \times 10^6$, and $\Theta = 1.014$.

(a) Wavenumber spectrum, averaged over the final 1000s.

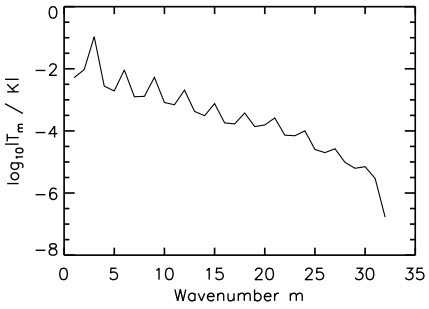

(b) $M = 3$ temperature amplitude time series.

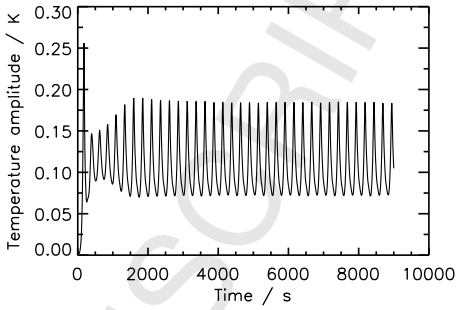

(c) $T_{M=3}(t)$ Fourier spectrum.

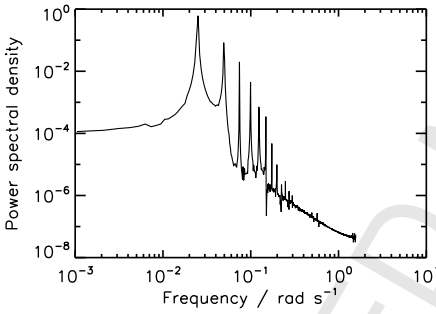

(d) $T_{M=3}(t)$ derivative coordinate reconstruction.

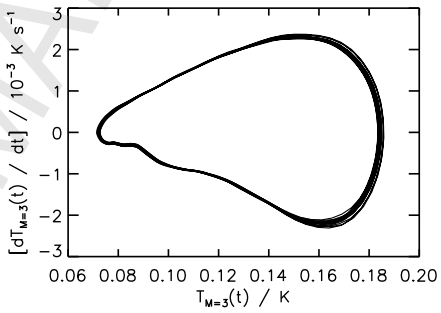

$2\pi/M$ radians (in the simpler regimes, at least). The wavenumber–M temperature amplitude time series $T_M(t)$ (Fig. 2b) shows the evolution of wave behaviour. A time series spectrum (Fig. 2c) defined by the Fourier transform of $T_M(t)$ after transients have decayed is useful, as each regime has a distinct spectral signature (N.B., as $T_M(t)$ is already the amplitude of a spatial Fourier transform, the drift frequency of the wave around the annulus is missing). Finally, the derivative coordinate reconstruction of $T_M(t)$ (Fig. 2d) also has a

distinct signature; its trajectory in phase space is given by

$$\begin{pmatrix} dT_M(t)/dt \\ \\ T_M(t) \end{pmatrix} \approx \begin{pmatrix} \left(T_{M,t+\Delta t} - T_{M,t-\Delta t}\right)/\left(2\Delta t\right) \\ \\ T_{M,t} \end{pmatrix},$$

where Δt is the time step size.

Figure 3 shows the full regime diagram and a region of detail. Approximate regime transitions are indicated by solid lines. As `MORALS` has been used for some 30 years it is surprising that a detailed diagram has not been constructed before now; rapid increases in computing power have now made it possible to do this. The simulations are still computationally expensive, however, each run taking 10–15 hours to complete [1].

3.1 Dynamical regimes

Six distinct regimes were observed: axisymmetric flow (AX), steady wave flow (S), amplitude vacillation (AV), modulated amplitude vacillation (MAV), structural vacillation (SV) and a previously unseen regime, period–doubled amplitude vacillation (AV–d). The boundary between steady wave flow and vacillating flow was defined using the vacillation index [3], defined as

$$I_V = \frac{\max(T_M) - \min(T_M)}{\max(T_M) + \min(T_M)}$$

To identify runs close to this boundary, two subdivisions of the steady wave regime have been defined, and the conditions for classifying runs in these

[1] The simulations were performed on an Open MOSIX cluster with nine Intel Netburst Xeon 2.8 GHz processors and 6GB RAM.

Fig. 3. Numerical regime diagram. In (a), each run is represented in the diagram by a number corresponding to its dominant wavenumber M, and in (b), by a point. Runs that do not fall into the regime of their immediate surroundings are indicated individually.

(a) Full

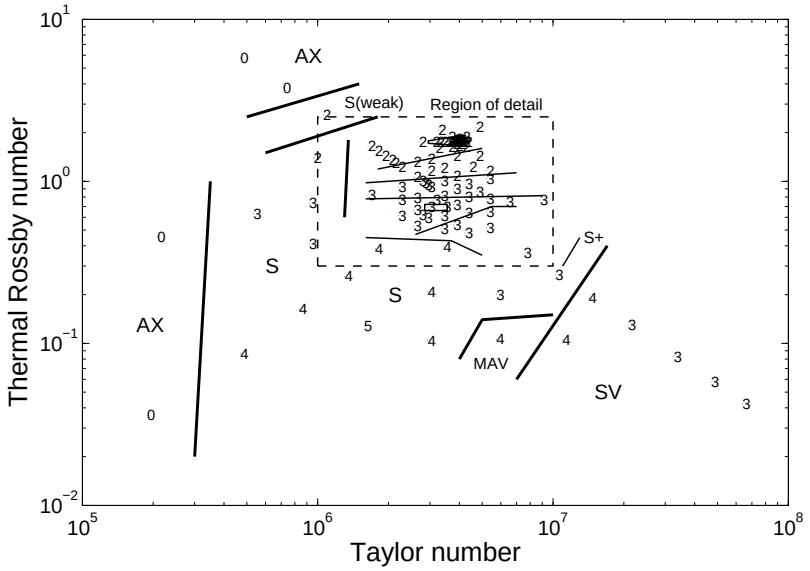

(b) Detail (dashed region above)

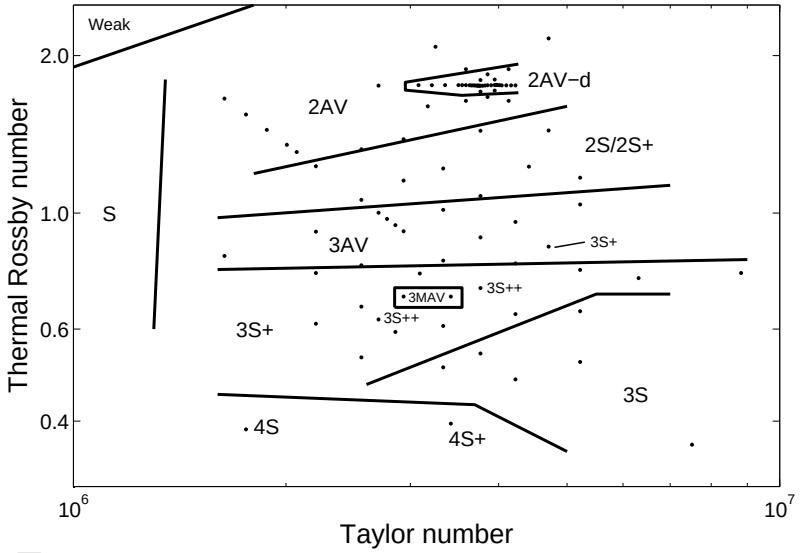

regimes are listed in Table 2. S++ effectively defines a flow right on the boundary between steady wave flow and vacillating flow.

Table 2

Classification of regimes based on vacillation index. $\langle I_V \rangle$ is the mean value of I_V over a time series (the mean of a set of I_V calculated using each pair of adjacent maxima and minima) and σ_{I_V} is its standard deviation.

$\langle I_V \rangle$	$\langle I_V \rangle + \sigma_{I_V}$	Classification
0	N/A	S
< 0.05	< 0.05	S+
< 0.05	≥ 0.05	S++
≥ 0.05	any	vacillating

The main features of Fig. 3 are similar to comparable regime diagrams obtained from laboratory work in the rotating annulus literature [1–3, 16–18]. **Axisymmetric** flow is observed at high Θ / low $\mathcal{T}$ and at low $\mathcal{T}$ (mid $\mathcal{T}$ / low Θ runs were not performed, so the boundary there could not be confirmed). This is distinguished by $M = 0$ in the wavenumber spectrum, and the absence of waves. In **steady wave** flow, one mode and its harmonics dominate the wavenumber spectrum; the amplitude of the dominant mode is constant; the derivative coordinate embedding deviates from a point only due to the limits of floating point precision, and the time series amplitude spectrum is smooth, tending to a maximum at low frequency. In **amplitude vacillation**, the dominant wave amplitude oscillates quasi-sinusoidally, and the strength of amplitude modulation is constant in time. One wave mode and its harmon-

ics dominate the wavenumber spectrum; the time series amplitude spectrum contains strong signals at the vacillation frequency and its harmonics, and the derivative coordinate embedding is periodic. Alternating steady wave and vacillating flows are observed with decreasing Ω, with each steady wave regime developing into AV before the transition to lower wavenumber. The S+ and S++ regions indicate the steady wave–vacillating transition is gradual. **Structural vacillation** was observed at high $\mathcal{T}$ / low Θ. Here the time series is aperiodic and its spectrum displays a noisy tail at high frequency, tending to a maximum at low frequency; in contrast to S and AV, the dominant mode and its harmonics in the wavenumber spectrum are only weakly dominant with respect to the other modes, and the derivative coordinate embedding is unstructured. The boundary between SV and irregular flows (geostrophic turbulence) is ambiguous and no attempt will be made to distinguish between flows in the two regimes here. Finally, Hide & Mason [19] define **'weak' waves** as flow where the mean value $A_M = \langle T_{M,peak-to-peak}(t) \rangle$ satisfies $A_M \lesssim 0.04\ \Delta T$, and 'strong' otherwise; these are waves whose amplitudes are nonzero despite having a thermal Rossby number above the Eady threshold for baroclinic instability. One run was defined as being 'weak' in this context. The amplitude of the wave in this case was highest at mid-R and mid-z, in contrast with [19] whose weak waves were confined to the vertical extremes of the domain.

3.2 Differences between simulation and laboratory

A number of differences were also found between Fig. 3 and laboratory results. Only a few flows exhibited **modulated amplitude vacillation** – in earlier laboratory work [3, 18] it was more common, although the fluid was of higher

Prandtl number. We define MAV here as a flow where the dominant wave amplitude oscillates at one frequency but the oscillation is modulated; the time series spectrum contains a strong peak at the vacillation frequency and at least one peak at lower frequency. The attractor traced in the derivative coordinate embedding has nonzero thickness. Steady regimes were found at low ΔT, and period doubled amplitude vacillation was seen at high ΔT (Section 4). None of the more exotic regimes seen by Früh & Read [18] in fluid of higher Prandtl number were found.

Early laboratory work [19] found that, when changing Ω at constant ΔT during a single experiment, in some situations the regime transitions occur at different rotation rates when increasing Ω, compared with decreasing Ω (the so–called 'hysteresis' effect). In our work each run used constant Ω, so it is not yet possible to determine whether this effect also occurs in numerical simulations of the annulus.

Hignett [2] used the same annulus dimensions and fluid as these simulations, so our regime diagram is the equivalent numerical version of that laboratory study. In addition to the similarities in Section 3.1 above, in both laboratory and numerical regime diagrams a similar sequence of behaviour was observed with increasing Ω along lines of constant ΔT, and transitions approximately follow lines of constant Θ. The Hignett regime diagram is confined to $2 \leq \Delta T/\ \mathrm{K} \leq 10$, so behaviour at low ΔT cannot be compared. The main difference between the two approaches is that wavenumber transitions are at lower Ω in our numerical results. For example, for $\Delta T = 4$ K the 2S/3AV transition occurs at $\Omega \approx 0.82$ rad s^{-1} in the laboratory, and at $\Omega \approx 0.71$ rad s^{-1} in our simulations, a shift of -0.11 rad s^{-1} from laboratory to model. This has previously been attributed to the presence of a thermocouple ring in the labo-

ratory setup [14]. Regime transitions are less clear at higher rotation rates, so it is impossible to say whether this shift is constant over the whole of $(\mathcal{T}, \Theta)$ space.

4 A sequence of bifurcations similar to the logistic map

Fig. 4. A regime diagram showing the runs performed to explore logistic map behaviour. The total time for each simulation was between 4500 and 13500 s, with $7.0 \leq \Delta T / \text{ K} \leq 11.5$ and $0.72 \leq \Omega \text{ / rad s}^{-1} \leq 0.90$. See text for further analysis of points A–D.

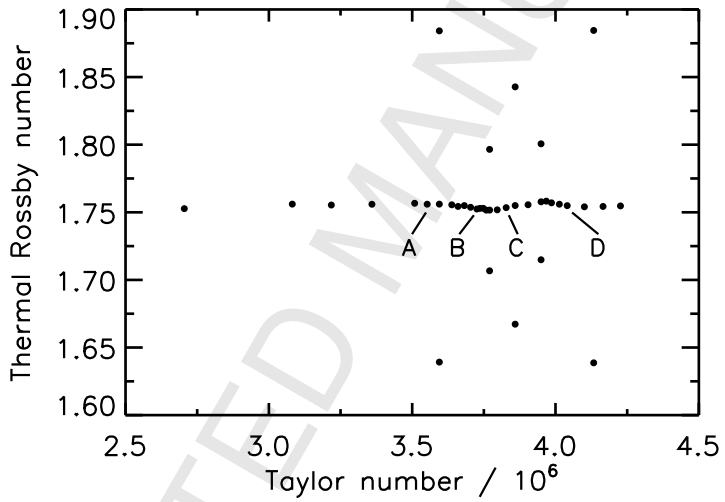

The area around $\Delta T = 10$ K, $\Omega = 0.86$ rad s^{-1} ($\mathcal{T} = 3.86 \times 10^6$, $\Theta = 1.755$) was explored at a higher resolution as the run at this point displayed behaviour not seen before. Fig. 4 shows the 37 runs performed in the region around this point. The main analysis was done along the line of 28 runs at $\Theta \approx 1.755$, and henceforth we shall focus only on these runs. Figures 5–8 show the results from four runs at points A–D along this sequence. Our attention was initially drawn to this behaviour by a time series similar to Fig. 7a, which is qualitatively

Fig. 5. Analysis of point A (2AV–dh, $\Omega = 0.8251$ rad s^{-1}, $\Delta T = 9.21$ K, $\mathcal{T} = 3.55 \times 10^6$, $\Theta = 1.756$) in Fig. 4. (a) $M = 2$ temperature time series; (b) time series spectrum derived from $T_{M=2}(t)$ after transients have decayed; (c) 2D projection of the delay coordinate trajectory reconstructed from the $T_{M=2}(t)$ time series in (a); (d) temperature maxima first return map.

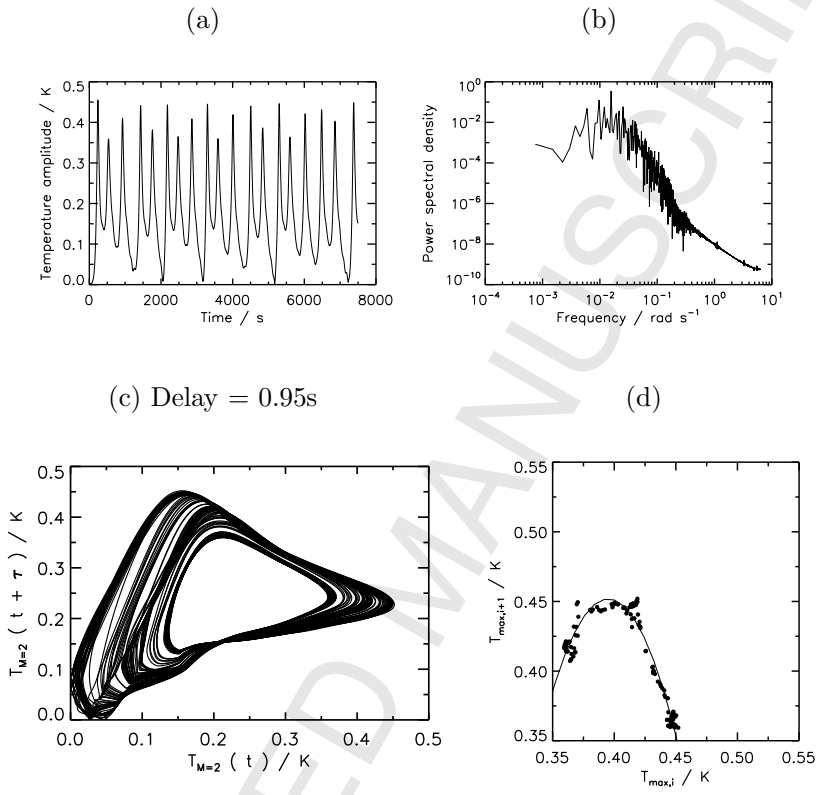

different from the amplitude vacillation in Fig. 2b. This difference is reinforced by comparing the frequency spectra of their amplitude time series: in Fig. 7b we see subharmonics below the main frequency, but these are not present in Fig. 2c, where only the harmonics are clear.

Qualitative features of this new behaviour can be visualized using delay coordinate reconstructions [20]. The D_E–dimensional delay coordinate reconstruction with delay τ of a scalar time series $(A_1,\ A_2,\ \ldots,\ A_{N-1},\ A_N)$ is

Fig. 6. As Fig. 5, but for point B (2AV–dh, $\Omega = 0.845$ rad s^{-1}, $\Delta T = 9.64$ K, $\mathcal{T} = 3.726 \times 10^6$, $\Theta = 1.752$).

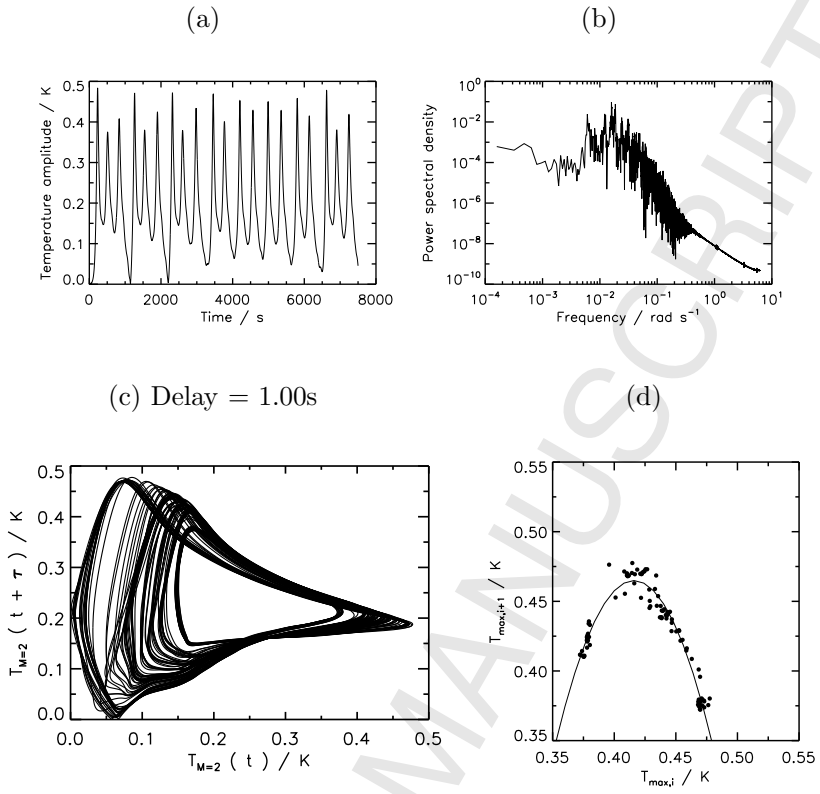

$$
\begin{array}{l}
(A_1,\ A_{1+\tau},\ A_{1+2\tau},\ \ldots,\ A_{1+(D_E-1)\tau}) \\
(A_2,\ A_{2+\tau},\ A_{2+2\tau},\ \ldots,\ A_{2+(D_E-1)\tau}) \\
\qquad\qquad \ldots\ldots \\
(A_I,\ A_{I+\tau},\ A_{I+2\tau},\ \ldots,\ A_{I+(D_E-1)\tau}).
\end{array}
$$

This defines a trajectory in phase space of length $I = N - \tau(D_E - 1)$. A number of conditions restrict the governing parameters [21]: small sampling time $t_s = t_{A_2} - t_{A_1}$ ensures a smooth approximation to the true trajectory, the delay time τ should be long enough to ensure independence between coordinates, and the embedding dimension D_E must be large enough to ensure a one–to–one map from time series to delay reconstruction.

In this work the sampling time was set such that $1.0 \leq t_s \ / \ \mathrm{s} \leq 2.5$ (over-

Fig. 7. As Fig. 5, but for point C (2AV–d3, $\Omega = 0.8565$ rad s^{-1}, $\Delta T = 9.91$ K, $\mathcal{T} = 3.83 \times 10^6$, $\Theta = 1.754$).

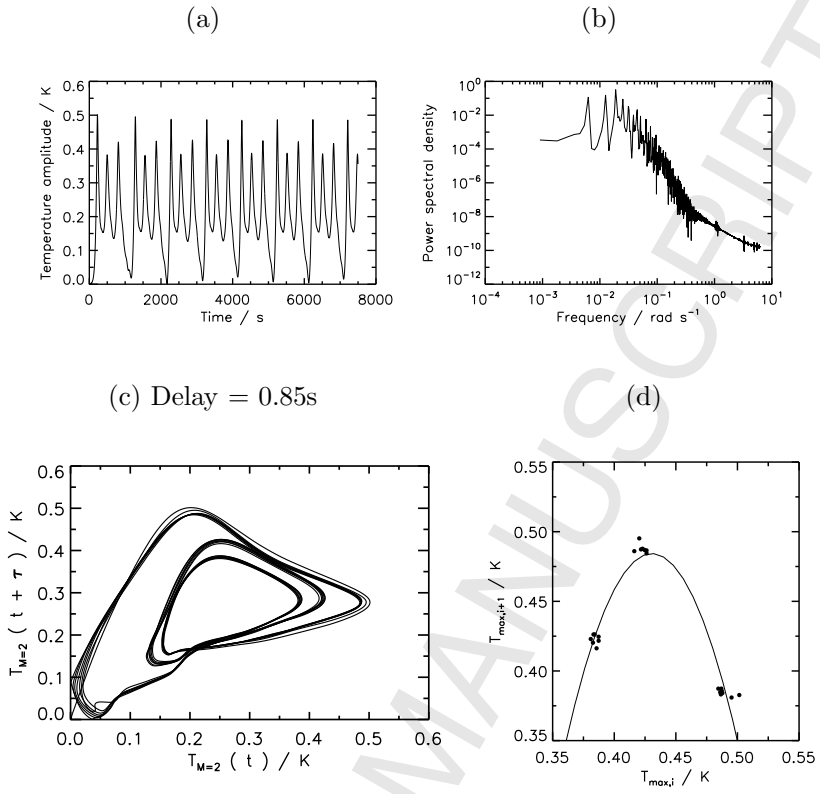

sampled, but at no extra computational cost). The embedding dimension was estimated using the method of false nearest neighbours [22], implemented using the *Nonlinear Time Series Analysis* (`TISEAN`) package [23, 24]; $D_E = 4$ was found to be suitable. The delay time was found by computing the first minimum of the time delayed mutual information [25], yielding values of 40 – 120 t_s (40 – 300 s).

Subfigures (c) in Figs 5–8 show four such reconstructions at points A–D. We define a new regime 'period–doubled amplitude vacillation' (2AV–d) for flows exhibiting multiple or aperiodic loops in their $M = 2$ delay coordinate reconstructions. The regime is further subdivided depending on the number of

Fig. 8. As Fig. 5, but for point D (2AV–d1, $\Omega = 0.88$ rad s^{-1}, $\Delta T = 10.47$ K, $\mathcal{T} = 4.04 \times 10^6$, $\Theta = 1.755$).

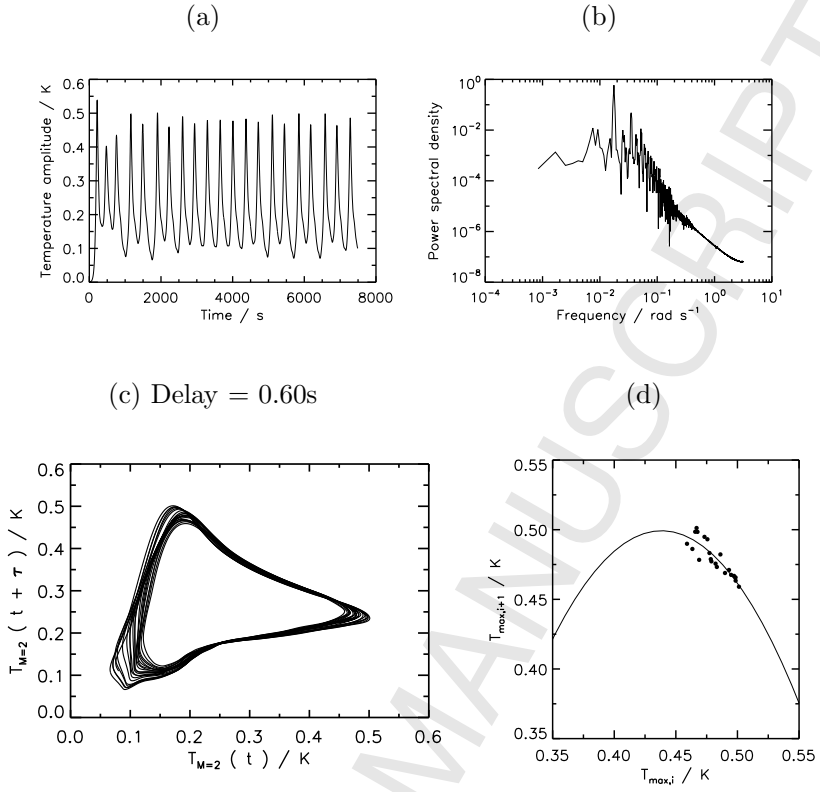

loops; we have observed 2AV–d1, 2AV–d2, 2AV–d3 for 1–3 loops respectively, and aperiodic regimes of higher order which we denote 2AV–dh. 2AV–d1 is distinguishable from 2AV by the width of the attractor in the delay coordinate reconstruction: 2AV is the limit of a single line, but this distinction is currently unquantified. Inspections of attractors A, B, and other 2AV–dh cases reveal a resemblance to the Rössler attractor [26] – in a 3D reconstruction, the shape is a mirror image. Schematically, it looks the same as Abraham & Shaw [27, p.94], except reflected about the vertical axis.

The presence of these different periods indicates some kind of bifurcation sequence. To quantify this, for each run the set of temperature amplitude max-

Fig. 9. Time series maxima of the $M = 2$ temperature mode for the 28 runs in Fig. 4. The maxima for each run are plotted at the appropriate Taylor number.

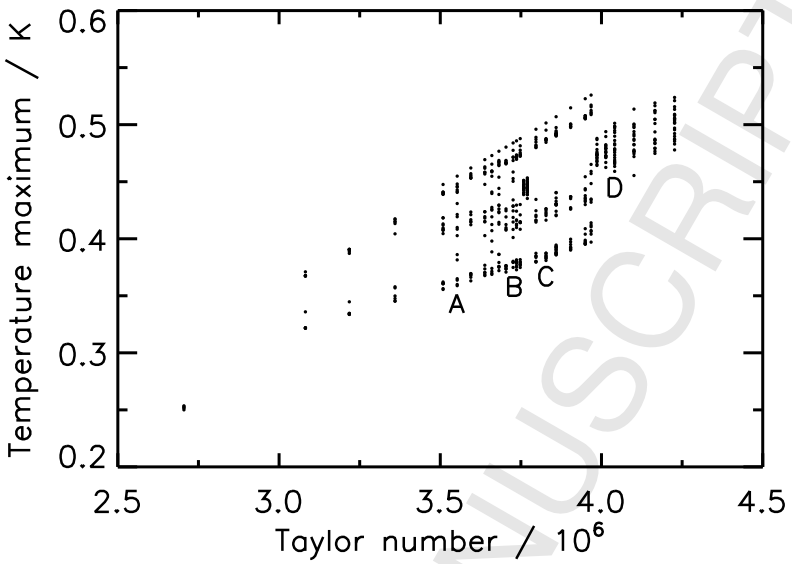

ima was identified in the $T_{M=2}(t)$ time series, and these temperatures are plotted in Fig. 9 against the corresponding Taylor number for each run. The result is similar to behaviour produced, for example, by bifurcations of the logistic map [5–7]. At low Taylor numbers the behaviour is periodic and bifurcates to 2AV–d2 with increasing Taylor number. Further bifurcations occur before A (2AV–dh), whose values are spread over the temperature range. Two periodic windows (2AV–d3) separate A from B (2AV–dh). By C (2AV–d3) periodic behaviour has returned. Around $\mathcal{T} \approx 4 \times 10^6$ an event occurs with results characteristic of a boundary crisis [28]. This causes the temperature range to tighten by a factor of 2–3, and periodicity is lost by D (2AV–d1).

The 2AV–d3 cases may imply that chaotic dynamics exist at certain intervals of Taylor number along the sequence [29]. It is also notable that the run to the left of A is 2AV–d3: this indicates that within the range $3.388 \times 10^6 \leq \mathcal{T} \leq 3.508 \times 10^6$ there should be a chaotic window, as the first period–3 window

for bifurcations of the logistic and similar maps occurs immediately after the first chaotic window.

We now consider whether a map similar to the logistic map exists to define the sequence of time series maxima in our simulations. In a continuous dynamical system $dX/dt = F(X)$, the first return map is constructed from a Poincaré section. For instance, this section can be an $(n-1)$–dimensional subspace $Y_i = (x_1, x_2, ..., x_{n-1})$ through an n–dimensional space $X_i = (x_1, x_2, ..., x_n)$ defined where x_n is constant: the first return map is then Y_{i+1} vs Y_i. In this context, we define the section using $x_n \equiv dT_{M=2}/dt = 0$. The first return map is $T_{\max,i+1}$ vs $T_{\max,i}$, where $T_{\max,i}$ is the ith maximum in the dominant wavenumber temperature time series $T_{M=2}(t)$. Subfigures (d) of Figs 5–8 show these maps for points A–D. For A and B in particular, a quadratic map

$$T_{\max,i+1} = \alpha + \beta T_{\max,i} + \gamma T_{\max,i}^2 \tag{1}$$

is a suitable fit, and the best fits are superimposed in all four cases. For 2AV–dh these fits are particularly good, indicating an underlying structure qualitatively similar to the logistic map.

4.1 A superposition of waves?

It is possible that this behaviour could be the produced by superimposing waves of incommensurate frequency, manifested in the dominant wavenumber at mid–height/mid–radius. We now argue that this is not the case, by showing that the oscillation of interest is present throughout the fluid, and is also present at other wavenumbers. To show that the oscillations are ubiquitous in space, the same spatial Fourier analysis was done at other points in the

Fig. 10. Further analysis of run B at five different points in the vertical slice: (a) time series of $M = 2$ temperature mode amplitudes at five different points. (R, z) positions are (in cm): α $(3.81, 11.12)$; β $(6.69, 11.12)$; γ $(5.25, 7.00)$; δ $(3.81, 2.88)$; ϵ $(6.69, 2.88)$; (b) positions of the five points in the slice; (c) time series showing Nusselt number at $R = a$.

(a) Time series

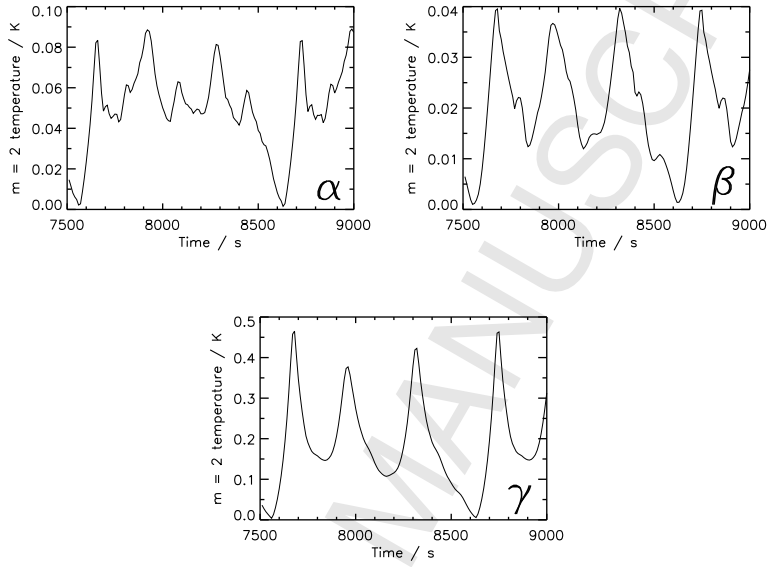

(b) Positions (to scale)

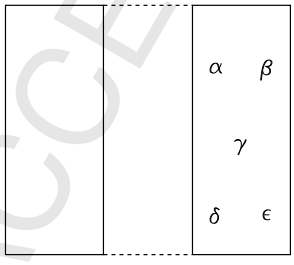

(c) Nusselt number

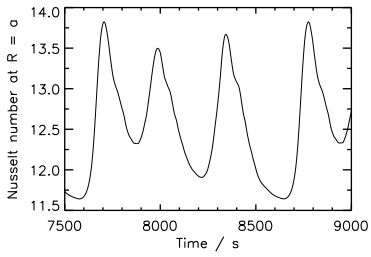

Fig. 11. The amplitudes of temperature modes $1 \leq m \leq 11$ at mid–height and mid–radius, as a function of time, for Run B. The temperature scale is logarithmic, from black [$\log_{10}(T_m/K) = -8.7$] to white [$\log_{10}(T_m/K) = -0.33$].

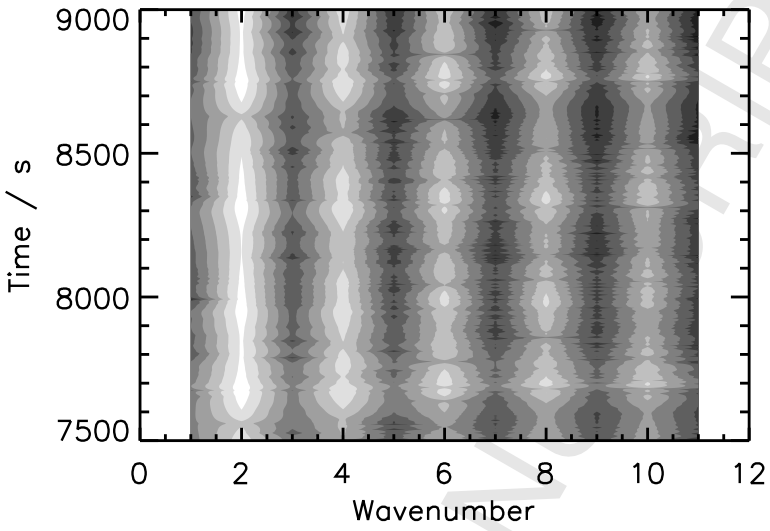

vertical slice, to add to the mid–radius/mid–height analysis done in Section 3. This was done for Runs A–D at four extra points over a short time window of 1500s in the middle of each run, and the results from Run B are shown in Fig. 10. Figure 10a shows part of the temperature mode $M = 2$ time series (Fig. 6a), along with four other points in the slice (positions shown in Fig. 10b). Similar oscillations to the central point are seen at the four other points, suggesting that the oscillation is present throughout the fluid. The positions of the maxima in time at each of points $\beta - \epsilon$ are the same (the range of times is at most 10s, which is the separation of individual points in time in Fig. 10a). The maxima at point α (low-R, high-z) lag behind the other four points by about 30s. Since this occurs in all four runs, including the 2AV-d1 case (which is the most similar to standard quasi–periodic 2AV), it would appear that this feature is typical of amplitude vacillating waves in the annulus.

The ubiquity of the oscillations as a nonlinear wave–zonal flow interaction can be confirmed by analyzing an equivalent time series for the Nusselt number at one of the sidewalls (Fig. 10c, for $R = a$, the inner sidewall). The Nusselt number is a dimensionless parameter that quantifies the importance of convective over conductive heat transfer, and is a single value summed over the whole sidewall. The evolution of the Nusselt number in Fig. 10c takes the same form as the temperature wave, which shows that the wave phenomenon being observed is present throughout the whole fluid. The peaks in the Nusselt number time series lag behind the temperature time series peaks by ~ 20s, but this is to be expected as information is passed from the fluid to the boundaries via heat transfer, not in the other direction. For brevity only the results from Run B are shown in the figure; the data from the other three runs give the same conclusions.

Superposition can also be ruled out by examining the time variation of other wavenumbers in the temperature field. In Fig. 11 the amplitudes of temperature wavenumbers 1 – 11 are shown graphically as a function of time, at mid-radius/mid–height for Run B (again over a short time window). The higher harmonics perform the same oscillations as the dominant mode (although with a small positive phase shift in the higher harmonics). These two results indicate that the wave behaviour observed here is a global oscillation, and not a superposition of multiple waves. The conclusions are the same for runs A, C, and D.

We now verify the connection with the logistic map using two further tests.

Fig. 12. First, second and third return maps for Runs A and B (left), compared with the equivalent return maps for the logistic map with (a) $r = 3.8$ and (b) $r = 3.87$.

(a) Run A: $\mathcal{T} = 3.556 \times 10^6$ (b) Run B: $\mathcal{T} = 3.724 \times 10^6$

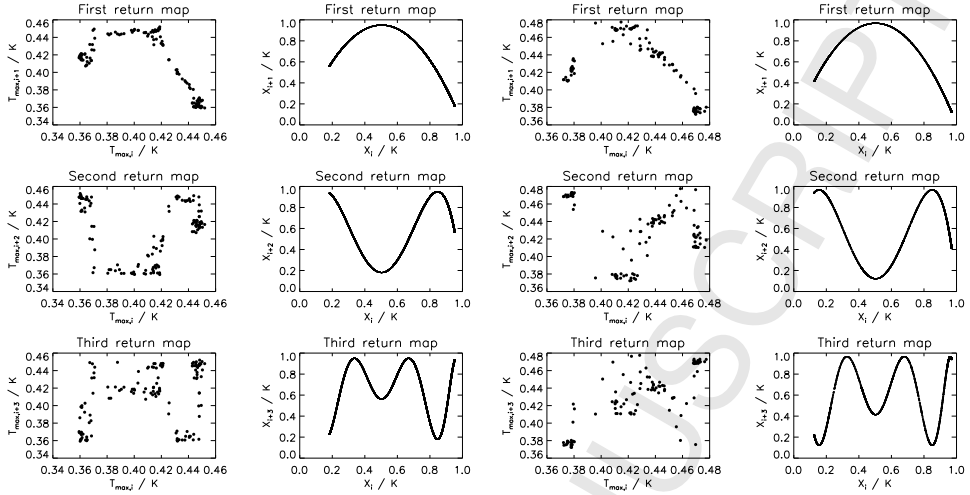

4.2 Higher order return maps

The runs at points A and B were extended to 53,408 s and 40,000 s respectively, to fill in their attractors and provide a larger number of maxima for the return maps than there were in the original runs (N.B.: for clarity, the plots in Figs 5 and 6 use the data from these longer runs, except in Figs 5a and 6a). Figure 12 shows the first, second and third return maps generated from these data (on the left), and on the right the corresponding return maps of the logistic map using $r = 3.8$ (run A) and $r = 3.87$ (run B). For all three return maps, the similarities between the data and the logistic map are clear.

4.3 Map predictions

The ultimate test of whether the map is useful or not is its ability to predict the next maximum in the series. For each maximum in the A and B time

series, the first return map fitted using Equation 1 was used to predict the next maximum in the sequence. The absolute error in these predictions was fairly uniformly spread between 0 K and 0.015 K with mean 0.0064 K for run A and between 0 K and 0.01 K with mean 0.0062 K for run B. Taking the size of the attractor to be the range in temperature covered by the maxima, this corresponds to an absolute mean error of 7% of the attractor size for run A, and 6% for run B. These values again confirm that the quadratic map is suitable to describe the sequence of temperature maxima.

5 Lyapunov exponents

Fig. 13. Lyapunov exponents calculated from the $T_{M=2}(t)$ time series for each simulation in Fig. 9.

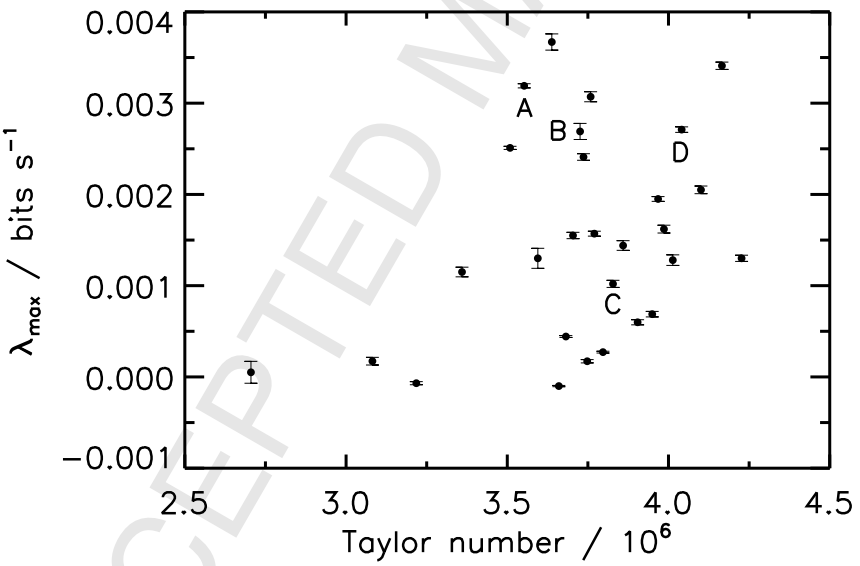

Finally, we verify that the 2AV–d flows in the bifurcation sequence are chaotic by computing estimates of their maximum Lyapunov exponents. If the dynamics follow the logistic map structure exactly, regimes 2AV–d1 through 2AV–d3

should not be chaotic and 2AV–dh should be chaotic. Deterministic systems with a single positive Lyapunov exponent $\lambda_{\max} > 0$ that display aperiodic long–term behaviour satisfy the conditions for chaos [30, p.323]. Wolf et al. [31] define the ith Lyapunov exponent as

$$\lambda_i = \lim_{t\to\infty}\left[\frac{1}{t}\log_2\left(\frac{p_i(t)}{p_i(0)}\right)\right],$$

where $p_i(t)$ is the length of the ith principal axis of the hyperellipsoid formed by deformation of an infinitesimal hypersphere under the action of a dynamical system. We use their algorithm to estimate the largest non–negative exponent of the time series $T_{M=2}(t)$. The algorithm itself calculates the exponent by first reconstructing the time series using a singular systems reconstruction [21, 32]. The exponent is then calculated from the long–term divergence of a pair of nearby orbits in the reconstructed phase space; the pair of starting points is chosen so that their separation in the original time series is at least one orbital period, to ensure the points are on different trajectories. When the separation between the trajectories reaches a particular length scale, or after a specified propagation time, a new point on the attractor is chosen close to the first trajectory along the line made between the two trajectories. By repeating this process, the long–term behaviour of a single principal axis vector is found.

In each case the exponent was measured by running the algorithm for embedding dimensions $3 \leq D_E \leq 7$; the maximum and minimum length scales were represented by 20% of the attractor diameter [peak to peak difference in $T_{M=2}(t)$] and 0.1% of the attractor diameter respectively, and a propagation time of 25% of the vacillation period was used. The exponent is the value that $\lambda_{\max}(t)$ asymptotically tends towards, where t is the length of the time series used to define the attractor (as $t \to \infty$ the whole attractor becomes available,

hence the asymptotic value of $\lambda_{\max}(t)$ is appropriate). If the plot did not contain such a region for this range in D_E, the calculation was repeated with a longer delay time. The exponent was then taken to be the mean value over the dimensions and ranges in time where this was satisfied (the plot for 2048 points in Fig. 10 of Wolf et al. [31] gives an example of an appropriately flat region).

The exponent was calculated for each of the 28 runs, and the results are shown in Fig. 13, plotted against Taylor number on the same horizontal scale as Fig. 9. The values are close to zero at low Taylor number, where period–1 and 2AV–d2 behaviour is observed. The rest of the plot is split into two regions of high $\lambda_{\max}$ near A and D (where the aperiodic behaviour is observed, now confirmed as chaotic by these exponents), and a region of lower $\lambda_{\max}$ near C, in the 2AV–d3 window. By comparison, $\lambda_{\max}$ calculated for a selection of AV and MAV runs in Fig. 3 is in the range $(-1.2 \times 10^{-4} \pm 3 \times 10^{-5}) \leq \lambda_{\max}/$ bits s^{-1} $\leq (6.3 \times 10^{-4} \pm 10^{-4})$, and for the SV runs it is $(1.3 \times 10^{-3} \pm 7 \times 10^{-5}) \leq \lambda_{\max}/$ bits s^{-1} $\leq (5.5 \times 10^{-3} \pm 2 \times 10^{-4})$. It should also be noted that the runs in the periodic windows of the bifurcation sequence have Lyapunov exponents an order of magnitude larger than the exponents for the AV and MAV runs.

We can connect these results with the map predictions in Section 4.3. The $\lambda_{\max}$ calculated here are of order 0.1 – 1.0 bits / orbit, where the orbital period is the vacillation period of the dominant wave mode (e.g. Fig. 2b). The error–doubling time is therefore a few orbits, so we would not expect even a near-perfect map to predict successive maxima with perfect precision. In this light, a mean error of only ∼6% in the predictions is encouraging.

6 Discussion

Behaviour resembling the logistic map has not been reported previously in the thermally-driven baroclinic rotating annulus, but there is a precedent elsewhere in the study of rotating fluids. Figures 6–8 of Hart [12] demonstrate period–doubling behaviour in a two layer open cylinder laboratory experiment driven by differential rotation, varying the 'friction parameter' at constant rotational Froude number (similar to varying $\mathcal{T}$ at constant Θ). Period–doubling has also been seen numerically in a number of truncated models [33, for example], but not in full models like this one.

Most of the literature on period–doubling in laboratory fluid systems is in the area of Rayleigh–Bénard convection [8–11]. Period–doubling is presented as one of a number of possible routes to chaos or turbulent convection, and is identified primarily through spectral analysis of time series. Similar analysis is possible here, but as the fine detail of parts of the sequence was not explored (particularly the bifurcations before the first chaotic window) this analysis is less conclusive. The appearance of subharmonics can be seen between Figs 2c and 7b: $f/3$ and $f/1.5$ are present in 7b but not in 2c. Evidence is limited elsewhere, however. Furthermore, the lack of runs in the region of the sequence where the initial bifurcations take place means that values of the Feigenbaum constants [6] cannot be calculated for our sequence. This is unfortunate, as they would allow further verification of the dynamics as well as comparison with the Rayleigh–Bénard system, where the data were accurate enough for these constants to be calculated.

It may be possible to observe period–doubled amplitude vacillation in the

laboratory in real annulus experiments. At the most crowded point along our sequence, the points differ in rotation rate by $\Delta\Omega \approx 0.002$ rad s^{-1}, and in temperature difference by $\Delta(\Delta T) \approx 0.05$ K. By comparison, laboratory rotation rates are typically stable to ± 0.0004 rad s^{-1}, and temperature differences to ± 0.02 K [34]. It may also be easier to derive the Feigenbaum constants using laboratory results, if similar methods to the Rayleigh–Bénard work are used.

In conclusion, the evidence from Figs 5–8, 9, and 12 strongly supports an underlying structure similar to the logistic map. It adds to the already rich range of behaviour observed in the rotating annulus over the years. A better quantitative analysis of this regime would require more simulations run for longer, but due to the time constraints imposed by the simulation this is computationally very expensive. Finally, the bifurcations we have described here are much simpler than the regime transitions that occur in the dynamical equations themselves; we have found evidence for an underlying simplicity in these complicated flows, which is an important step towards understanding them more generally.

RMBY acknowledges support via NERC Studentship NER/S/A/2005/13667, and thanks A. A. Castrejón–Pita for a useful suggestion during revision. We also wish to thank two anonymous reviewers for their comments.

A MORALS's equations of state

The equations solved by `MORALS` are closed by an equation of state $\rho(T)$, and two 'constitutive' relations for diffusion coefficients ν and κ:

Viscosity / 10^{-2} cm^2 s^{-1}:

$$\nu = 1.620\left[1 - 2.790\times10^{-2}(T-T_R) + 6.730\times10^{-4}(T-T_R)^2\right] \quad \text{(A.1)}$$

Density / g cm^{-3}:

$$\rho = 1.043\left[1 - 3.070\times10^{-4}(T-T_R) - 7.830\times10^{-6}(T-T_R)^2\right] \quad \text{(A.2)}$$

Thermal diffusivity / 10^{-3} cm^2 s^{-1}:

$$\kappa = 1.290\left[1 + 2.330\times10^{-3}(T-T_R)\right] \quad \text{(A.3)}$$

$T_R = 22°$C in each case.

References

[1] R. Hide, P. J. Mason, Sloping convection in a rotating fluid, Adv. Phys. 24 (1) (1975) 47–100.

[2] P. Hignett, Characteristics of Amplitude Vacillation in a Differentially Heated Rotating Fluid Annulus, Geophys. Astrophys. Fluid Dyn. 31 (3–4) (1985) 247–281.

[3] P. L. Read, M. J. Bell, D. W. Johnson, R. M. Small, Quasi–periodic and chaotic flow regimes in a thermally driven, rotating fluid annulus, J. Fluid Mech. 238 (1992) 599–632.

[4] C. E. Newman, P. L. Read, S. R. Lewis, Investigating atmospheric predictability on Mars using breeding vectors in a general–circulation model, Q. J. R. Meteorol. Soc. 130 (2004) 2971–2989.

[5] R. M. May, Simple mathematical models with very complicated dynamics, Nature (London) 261 (5560) (1976) 459–467.

[6] M. J. Feigenbaum, Quantitative Universality for a Class of Nonlinear Transformations, J. Stat. Phys. 19 (1) (1978) 25–52.

[7] M. J. Feigenbaum, The onset spectrum of turbulence, Phys. Lett. 74A (6) (1979) 375–378.

[8] J. P. Gollub, S. V. Benson, Many routes to turbulent convection, J. Fluid Mech. 100 (3) (1980) 449–470.

[9] M. Giglio, S. Musazzi, U. Perini, Transition to Chaotic Behavior via a Reproducible Sequence of Period–Doubling Bifurcations, Phys. Rev. Lett. 47 (4) (1981) 243–246.

[10] A. Libchaber, C. Laroche, S. Fauve, Period doubling cascade in mercury, a quantitative measurement, J. Phys. Lett. (Paris) 43 (7) (1982) L211–L216.

[11] J. A. Glazier, M. H. Jensen, A. Libchaber, J. Stavans, Structure of Arnold tongues and the f(α) spectrum for period doubling: Experimental results, Phys. Rev. A 34 (2) (1986) 1621–1624.

[12] J. E. Hart, A laboratory study of baroclinic chaos on the f–plane, Tellus 37A (3) (1985) 286–296.

[13] L. Farnell, R. A. Plumb, 'Numerical integration of flow in a rotating annulus II: three dimensional model', Occasional Note Met O 21 76/1, GFD Laboratory, UK Meteorological Office, 1976 (unpublished).

[14] P. Hignett, A. A. White, R. D. Carter, W. D. N. Jackson, R. M. Small, A comparison of laboratory measurements and numerical simulations of baroclinic wave flows in a rotating cylindrical annulus, Q. J. R. Meteorol. Soc. 111 (467) (1985) 131–154.

[15] P. L. Read, N. P. J. Thomas, S. H. Risch, An Evaluation of Eulerian and Semi–Lagrangian Advection Schemes in Simulations of Rotating, Stratified Flows in the Laboratory. Part I: Axisymmetric Flow, Mon. Weather Rev. 128 (8) (2000)

2835–2852.

[16] D. Fultz, R. R. Long, G. V. Owens, W. Bohan, R. Kaylor, J. Weil, Studies of thermal convection in a rotating cylinder with some implications for large–scale atmospheric motions, Meteorol. Monogr. 4 (21) (1959) 1–104.

[17] W. W. Fowlis, R. Hide, Thermal Convection in a Rotating Annulus of Liquid: Effect of Viscosity on the Transition Between Axisymmetric and Non–Axisymmetric Flow Regimes, J. Atmos. Sci. 22 (5) (1965) 541–558.

[18] W.-G. Früh, P. L. Read, Wave interactions and the transition to chaos of baroclinic waves in a thermally driven rotating annulus, Phil. Trans. R. Soc. A 355 (1722) (1997) 101–153.

[19] R. Hide, P. J. Mason, On the Transition Between Axisymmetric and Non–Axisymmetric Flow in a Rotating Liquid Annulus Subject to a Horizontal Temperature Gradient, Geophys. Astrophys. Fluid Dyn. 10 (3) (1978) 121–156.

[20] N. H. Packard, J. P. Crutchfield, J. D. Farmer, R. S. Shaw, Geometry from a Time Series, Phys. Rev. Lett. 45 (9) (1980) 712–716.

[21] D. S. Broomhead, G. P. King, Extracting qualitative dynamics from experimental data, Physica 20D (1986) 217–236.

[22] M. B. Kennel, R. Brown, H. D. I. Abarbanel, Determining embedding dimension for phase–space reconstruction using a geometrical construction, Phys. Rev. A 45 (6) (1992) 3403–3411.

[23] R. Hegger, H. Kantz, T. Schreiber, Practical implementation of nonlinear time series methods: The TISEAN package, CHAOS 9 (2) (1999) 413–435.

[24] H. Kantz, T. Schreiber, Nonlinear Time Series Analysis, 2nd Edition, Cambridge University Press, 2004.

[25] A. M. Fraser, H. L. Swinney, Independent coordinates for strange attractors from mutual information, Phys. Rev. A 33 (2) (1986) 1134–1140.

[26] O. E. Rössler, An equation for continuous chaos, Phys. Lett. 57A (5) (1976)

397–398.

[27] R. H. Abraham, C. D. Shaw, Dynamics – The Geometry of Behavior. Part Two: Chaotic Behavior, The Visual Mathematics Library: Vismath Volume 2, Aerial Press Inc., Santa Cruz, CA, 1983.

[28] C. Grebogi, E. Ott, J. A. Yorke, Crises, sudden changes in chaotic attractors, and transient chaos, Physica 7D (1–3) (1983) 181–200.

[29] T.-Y. Li, J. A. Yorke, Period three implies chaos, Am. Math. Mon. 82 (10) (1975) 985–992.

[30] S. H. Strogatz, Nonlinear Dynamics and Chaos, Studies in Nonlinearity, Perseus Books Publishing LLC, 1994.

[31] A. Wolf, J. B. Swift, H. L. Swinney, J. A. Vastano, Determining Lyapunov exponents from a time series, Physica 16D (1985) 285–317.

[32] P. L. Read, Applications of singular systems analysis to 'Baroclinic chaos', Physica D 58 (1–4) (1992) 455–468.

[33] S. Koo, M. Ghil, Successive bifurcations in a simple model of atmospheric zonal–flow vacillation, CHAOS 12 (2) (2002) 300–309.

[34] A. A. Castrejón-Pita, P. L. Read, Baroclinic waves in an air–filled thermally driven rotating annulus, Phys. Rev. E 75 (1) (2007) 026301.